Reassessment of the temperature-emissivity separation from multispectral thermal infrared data: Introducing the impact of vegetation canopy by simulating the cavity effect with the SAIL-Thermique model

Frédéric Jacob, Audrey Lesaignoux, Albert Olioso, Marie Weiss, Karine Caillault, Stéphane Jacquemoud, Françoise Nerry, Andrew French, Thomas Schmugge, Xavier Briottet, et al.

Reassessment of the temperature-emissivity separation from multispectral thermal infrared data: Introducing the impact of vegetation canopy by simulating the cavity effect with the SAIL-Thermique model

Frédéric Jacob [a,*], Audrey Lesaignoux [a], Albert Olioso [b], Marie Weiss [b], Karine Caillault [c], Stéphane Jacquemoud [d], Françoise Nerry [e], Andrew French [f], Thomas Schmugge [g], Xavier Briottet [h], Jean-Pierre Lagouarde [i]

[a] *IRD/UMR LISAH, Montpellier, France*
[b] *UMR EMMAH, INRA, UAPV, Avignon, France*
[c] *ONERA/DOTA, Palaiseau, France*
[d] *Université Paris Diderot/UMR IPGP, Paris, France*
[e] *CNRS/UMR ICUBE, Illkirch, France*
[f] *USDA/ARS/ALARC, Maricopa, AZ, USA*
[g] *NM Water Resources Institute, NMSU, Las Cruces, NM, USA*
[h] *ONERA/DOTA, Toulouse, France*
[i] *INRA/UMR ISPA, Villenave d'Ornon, France*

We investigated the use of multispectral thermal imagery to retrieve land surface emissivity and temperature. Conversely to concurrent methods, the temperature emissivity separation (TES) method simply requires single overpass without any ancillary information. This is possible since TES makes use of an empirical relationship that estimates the minimum emissivity ε-min from the emissivity spectral contrast captured over several channels, so-called maximum-minimum difference (MMD). In previous studies, the ε-min - MMD empirical relationship of TES was calibrated and validated for various sensor spectral configurations, where the proposed calibrations involved single or linearly mixed spectra of emissivity at the leaf or soil level. However, cavity effect should be taken into account at the vegetation canopy level, to avoid an underestimation of emissivity, especially for intermediate vegetation conditions between bare soil and full vegetation cover.

The current study aimed to evaluate the performances of the TES method when applied to vegetation canopies with cavity effect. We used the SAIL-Thermique model to simulate a library of emissivity spectra for a wide range of soil and plant conditions, and we addressed the spectral configurations of recent and forthcoming sensors. We obtained good results for calibration and validation over the simulated library, except for full cover canopies because of the TES gray body problem. Consistent with previous studies, the calibration/validation results were better with more channels that capture emissivity spectral contrast more efficiently. Our TES calibrations provided larger ε-min values as compared to former studies, especially for intermediate vegetation cover. We explained this trend by the simulated spectral library that involved numerous vegetation canopies with cavity effect, thereby shifting up the ε-min - MMD empirical relationship. Consequently, our TES calibration provided larger (respectively lower) estimates of emissivity (respectively radiometric temperature) that were likely to be more realistic as compared to previous calibrations. Finally, SAIL-Thermique simulations permitted to show that increasing Leaf Area Index induced a displacement of the (ε-min, MMD) pairs along the empirical relationship. This was consistent with the TES underlying assumption, where any change in ε-min induces changes in MMD since ε-max is bounded on [0.98–1]. Further investigations should focus on validating the outcomes of the current study against ground-based measurements, and on assessing TES performances when accounting for instrumental and atmospheric perturbations.

1. Introduction

Land surface temperature is a key environmental variable that drives several land surface processes, including radiation budget (Hulley and Hook, 2011; Ogawa et al., 2003), heat and water exchanges within

* Corresponding author at: 2 Place Pierre Viala, 34060 Montpellier Cedex 1, France.
E-mail address: frederic.jacob@ird.fr (F. Jacob).

surface boundary layer (Chehbouni et al., 2008; Schröder et al., 2006; Vinukollu et al., 2011), soil water depletion though evaporation and transpiration (Anderson et al., 2012; Er-Raki et al., 2008; Galleguillos et al., 2011; Kalma et al., 2008; Olioso et al., 1996; Pardo et al., 2014), vegetation photosynthesis and soil respiration (Inoue et al., 2004; Olioso et al., 2005), pollutant degradation (Louchart and Voltz, 2007), or pathogen dissemination (Courault et al., 2009). Given the implications for the related environmental issues, multi-decadal monitoring of land surface temperature has been recognized as a priority specification for recent satellite missions devoted to Earth observation (Green et al., 2012; Lagouarde et al., 2013; Malenovský et al., 2012; Murphy, 2006; Roy et al., 2014; Schmit et al., 2005).

Various difficulties have to be overcome when recovering land surface temperature from remote sensing data collected over the thermal infrared (TIR) spectral domain (Dash et al., 2002; Jacob et al., 2008; Jacob and Weiss, 2014; Li et al., 2013). One challenging task is to separate land surface emissivity and radiometric temperature by solving an undetermined problem with N equations (N waveband measurements) and N + 1 unknowns (N waveband emissivities and one radiometric temperature). Besides, solving this undetermined problem requires accounting for the coupling of atmospheric emission with land surface reflectance, the latter being often assumed equal to 1-emissivity.

Various methods have been proposed to separate land surface emissivity and radiometric temperature (Dash et al., 2002; Jacob et al., 2008; Li et al., 2012). They rely on using the spectral, angular and temporal information collected from remotely sensed data, and may require prior atmospheric corrections or not. The first group of methods consists of combining data from one or two TIR channels along with data from visible and near infrared channels (Jiménez-Muñoz et al., 2014). The second group of methods consists of combining the spectral, angular and temporal information collected over the TIR domain and optionally over the middle infrared domain (Petitcolin and Vermote, 2002; Wan and Li, 1997). The third group of methods consists of using the spectral information captured with TIR multispectral/hyperspectral data (Barducci and Pippi, 1996; Payan and Royer, 2004; Schmugge et al., 2002). As compared to the methods belonging to the first two groups, those of the third group use single overpasses only while minimizing the dependency upon ancillary information, which is interesting over land surfaces that depict temporal dynamics in temperature and spatial heterogeneities.

Separating emissivity and temperature from TIR multispectral data consists of estimating waveband emissivity for a given channel to next retrieve all the waveband emissivities and the radiometric temperature. Normalized emissivity method (NEM) aims to accurately quantify emissivity variations, by arbitrarily setting the maximum emissivity (Coll et al., 2002), whereas adjusted NEM (ANEM) makes use of vegetation cover fraction to improve the setting of maximum emissivity (Coll et al., 2003). The temperature emissivity separation (TES) approach consists of estimating minimum emissivity from the emissivity spectral contrast captured with multispectral measurements (Gillespie et al., 1998; Schmugge et al., 1998). As compared to NEM and ANEM, TES does not rely neither on arbitrary setting of emissivity nor on ancillary information, but on an empirical relationship between minimum emissivity ε-min and emissivity spectral contrast. The latter is estimated as the ratio of emissivity range to emissivity mean value, the so-called maximum - minimum difference (MMD).

Many studies investigated the retrieval performances of TES, by focusing either on calibration (Grigsby et al., 2015; Hulley, 2011; Hulley et al., 2014; Hulley and Hook, 2011; Jimenez-Munoz et al., 2014; Payan and Royer, 2004; Sobrino and Jiménez-Muñoz, 2014) or on retrieval accuracies (French et al., 2008; Gillespie et al., 2011; Göttsche and Hulley, 2012; Hulley et al., 2012b; Jacob et al., 2004; Jiménez-Muñoz et al., 2006; Jimenez-Munoz et al., 2014; Mira et al., 2009, 2011; Sabol et al., 2009; Sobrino et al., 2007). These studies addressed several issues among which (1) the calibration of the ε-min - MMD relationship for different sensor spectral configurations, (2) the robustness of the ε-min - MMD relationship and the TES retrieval performances with regards to emissivity variations depicted by land surfaces, and (3) the impact of experimental errors (e.g., instrumental and atmospheric perturbations) on the accuracy of TES emissivity/temperature retrievals. All calibration studies relied on emissivity spectra derived from single or linearly mixed samples of soil/leaf spectra, without accounting for the characteristics of radiative transfer within vegetation canopy.

The use of single or linearly mixed samples of soil/leaf spectra induces an underestimation of land surface emissivity in a large range of situations (Olioso et al., 2014). This underestimation is explained by the cavity effect that results from radiation trapping within vegetation canopy: multiple scattering combined with large leaf absorptance induce larger emissivity for vegetation canopy as compared to single leaf (Anton and Ross, 1990; Chen et al., 2004; Francois et al., 1997; Guillevic et al., 2003; Merlin and Chehbouni, 2004; Olioso, 1995; Olioso et al., 2007). In most cases, land surface emissivity increases as the amount of aboveground vegetation increases (e.g., van de Griend and Owe, 1993). In case of low leaf emissivity due to leaf dryness, land surface emissivity can decrease as the amount of aboveground vegetation increases, but it is still larger than leaf emissivity (Olioso et al., 2007). The cavity effect is neither constant nor proportional to the vegetation amount. At low vegetation cover, canopy emissivity increases rapidly with vegetation amount and next follows an asymptotic behavior towards the highest level of cavity effect. This induces the classical non-linear relationship between normalized difference vegetation index (NDVI) and land surface emissivity (e.g., Olioso, 1995; van de Griend and Owe, 1993). Vegetation leaves depict large emissivity values (>0.9), so that saturation effect occurs at intermediate leaf area index (around 3–4) that correspond to intermediate NDVI values (around 0.6–0.7). Therefore, the calibration of the ε-min - MMD empirical relationship may be critical when using single or linearly mixed samples of soil/leaf spectra, because of cavity effect within canopy, especially for intermediate vegetation cover.

The current study aimed to evaluate the performances of the TES method when applied to vegetation canopies with cavity effect. We addressed the canopy level without any consideration of atmospheric or instrumental perturbations. Since emissivity spectra for land surfaces including plant canopies were not available in the existing spectral libraries, we used the SAIL-Thermique model (Olioso, 1992; Olioso, 1995) to simulate emissivity spectra for a wide range of soil and plant canopy conditions. We investigated two critical issues applying TES over vegetation canopies. We first addressed the calibration/validation of the ε-min - MMD relationship over the library of simulated spectra, by addressing the spectral configurations of recent and forthcoming sensors. Then, we evaluated the interest of using the SAIL-Thermique simulated dataset of emissivity spectra, by comparing the corresponding calibration/validation results with those obtained in former studies based on single or linearly mixed samples of soil/leaf spectra.

Section 2 presents the TES concept. Section 3 presents the methodological strategy, including the set-up of an emissivity spectral library by using the SAIL-Thermique model (Section 3.1), the set-up of a library of surface outgoing radiance (Section 3.2), the computation of the waveband quantities for different spectral configurations corresponding to various sensors (Section 3.3), as well as the calibration of the ε-min - MMD relationship and the validation of TES retrievals against original prescriptions (Section 3.4). Section 4 reports the results, including the calibration of the ε-min - MMD relationship (Section 4.1), the validation of the TES retrievals (Section 4.2), and the interest of using SAIL-Thermique simulations of emissivity spectra as compared to the use of single or linearly mixed samples of soil/leaf spectra (Section 4.3). Section 5 discusses the results in the light of former studies. Finally, concluding remarks highlight the main outcomes, the current investigations and the future challenges.

2. The TES concept: linking minimum emissivity and emissivity spectral contrast

We give here an overview of the TES method, by focusing on the key points that are relevant for the current study. Detailed descriptions can be found in Gillespie et al. (1998); Schmugge et al. (1998) and Schmugge et al. (2002). Hereafter, emissivity and radiance values correspond to waveband values over channels.

TES was originally designed to make use of the emissivity spectral contrast captured from multispectral remote sensing data over the TIR spectral domain. The undetermined problem related to the recovering of N + 1 unknowns (N emissivities and radiometric temperature) from N equations (measurements of surface outgoing radiance over N channels) is solved by empirically relating the minimum emissivity ε-min to the emissivity spectral contrast captured over the N channels. In order to reduce experimental noises that stem from instrumental and atmospheric perturbations, emissivity spectral contrast is characterized using the maximum minimum difference (MMD). MMD is the ratio of the emissivity range over the channels (difference between the maximum and minimum emissivity values, ε-max − ε-min) to the mean emissivity value ε-mean (Gillespie et al., 1998). Once ε-min is estimated, emissivity for any channel can be retrieved along with radiometric temperature. This relies on the calculation of surface outgoing radiance as the sum of (1) the emission component driven by surface emissivity and radiometric temperature and (2) the reflection component driven by atmospheric downwelling irradiance and surface reflectance (assumed equal to 1-emissivity).

The empirical relationship between minimum emissivity and MMD is a power function: $\varepsilon\text{-min} = A + B \times MMD^C$. Given the importance of estimating ε-min that is the first step for retrieving N emissivities and radiometric temperature, a special attention has been paid to the calibration of this empirical relationship. Gillespie et al. (1998) first proposed a calibration for earth observation system (EOS)/advanced spaceborne thermal emission and reflection radiometer (ASTER) using five channels. Several studies have subsequently proposed calibrations for the spectral configurations of various sensors such as EOS/moderate resolution imaging spectroradiometer (MODIS) with three channels (Hulley et al., 2014; Hulley and Hook, 2011; Jimenez-Munoz et al., 2014), EOS/ASTER with three channels close to the MODIS ones (Hulley and Hook, 2011), hyperspectral infrared imager (HyspIRI) with six channels (Hulley, 2011), MODIS/ASTER simulator (MASTER) with five channels close to HyspIRI ones (Grigsby et al., 2015), or Meteosat second generation (MSG)/spinning enhanced visible and infrared image (SEVIRI) with three channels (Jimenez-Munoz et al., 2014). Overall, calibrated coefficients vary greatly from one sensor to another, with relative changes in A, B and C values up to 15–20% relative, and with subsequent changes in ε-min value up to 0.015 (respectively 0.025) for a MMD value of 0.1 (respectively 0.3).

3. Applying TES over vegetation canopies by using radiative transfer modeling

To simulate emissivity spectra of vegetation canopies for a wide range of soil and plant conditions, we used the SAIL-Thermique model that mimics radiative transfer within the canopy by accounting for radiation trapping and subsequent cavity effect. We next calculated spectra of surface outgoing radiance from (1) the emissivity spectra simulated with SAIL-Thermique, (2) prescribed values of radiometric temperature, and (3) spectra of atmospheric downwelling irradiance. We finally calculated waveband values of emissivity, atmospheric downwelling irradiance and surface outgoing radiance, by convolving the corresponding spectra with the channel filters of existing and forthcoming sensors.

Prior to the calculation of radiance/irradiance spectra and of waveband values, the library of emissivity spectra was split into two equal parts. The first part, referred to as calibration dataset hereafter, was used to calibrate the TES empirical relationship, i.e. to adjust the (A, B, C) coefficients of the ε-min - MMD relationship. The second part, referred to as validation dataset hereafter, was used to (1) apply TES on waveband values of surface outgoing radiance, and (2) compare TES retrievals of radiometric temperature and emissivities against original prescriptions. The robustness of the coefficient estimation by means of randomization was a posteriori confirmed, since the variability of the calibrated coefficients was about 1–2% relative when repeating the procedure 100 times.

We detail hereafter the different methodological steps, where emissivity and radiance values correspond to waveband values for given channels, except when indicated for a specific wavelength. Fig. 1 displays a flowchart of the procedure.

3.1. Setting up a library of emissivity spectra with radiative transfer modeling

Conducting simulations with the SAIL-Thermique model, presented in Section 3.1.1, required the gathering of the model inputs (Section 3.1.2), the design of the model simulations (Section 3.1.3), and the filtering of simulated emissivity spectra to avoid redundancies in spectral behavior (Section 3.1.4). We did not add any noise to the simulations, since we addressed the canopy level without any consideration of atmospheric or instrumental perturbations that impact at-sensor radiance.

3.1.1. The SAIL-Thermique radiative transfer model

The scattering by arbitrarily inclined leaves (SAIL) model was originally developed by Verhoef (1984, 1985) to simulate land surface reflectance over the solar domain. SAIL describes any land surface as a turbid medium that includes a soil substrate beneath a homogeneous vegetation layer, possibly extended to a stack of vegetation layers. SAIL describes vegetation canopy thanks to leaf optical properties and prescribed canopy structure (i.e., LAI for leaf area index and LIDF for leaf inclination distribution function). The radiative transfer equations on which SAIL relies account for successive radiation scattering (reflection, transmission, absorption) within the canopy and between the canopy and the soil.

The SAIL-Thermique model was adapted from the original SAIL model by Olioso (1992) and Olioso (1995) to simulate vegetated land surface emissivities using the SAIL underlying physics. SAIL-Thermique permits to simulate radiative transfer over the TIR domain and thus to compute emissivity or directional brightness temperature. The simulation of land surface emissivity between 8 and 14 μm was demonstrated by Olioso et al. (2007) and Olioso et al. (2014). Verhoef et al. (2007) also favorably compared SAIL-Thermique against the 4SAIL model.

SAIL-Thermique considers the Kirchhoff's law at the thermodynamical equilibrium. It assumes that surface emissivity in any direction can be calculated as surface absorptance for the radiation originating from this direction. Then, the spectral emissivity ε_λ is computed from the simulated directional-hemispherical reflectance ϱ_λ: $\varepsilon_\lambda = 1 - \varrho_\lambda$, thus corresponding to directional r-emissivity (Norman and Becker, 1995).

To compute directional-hemispherical reflectance, SAIL-Thermique requires information about (1) the optical properties of the canopy components: soil reflectance spectra, leaf reflectance spectra and leaf transmittance spectra; (2) vegetation structure: LAI and LIDF for each vegetation layer, and (3) view zenith angle for the considered sensor. We explain in the next section how this information was obtained.

3.1.2. SAIL-Thermique inputs: spectral libraries of soil and leaf optical properties

Only few leaf data including reflectance and transmittance spectra were available. We used data from five soil spectral libraries and one leaf spectral library. These spectra were obtained from laboratory measurements over soil and leaf samples, using TIR spectrometry combined

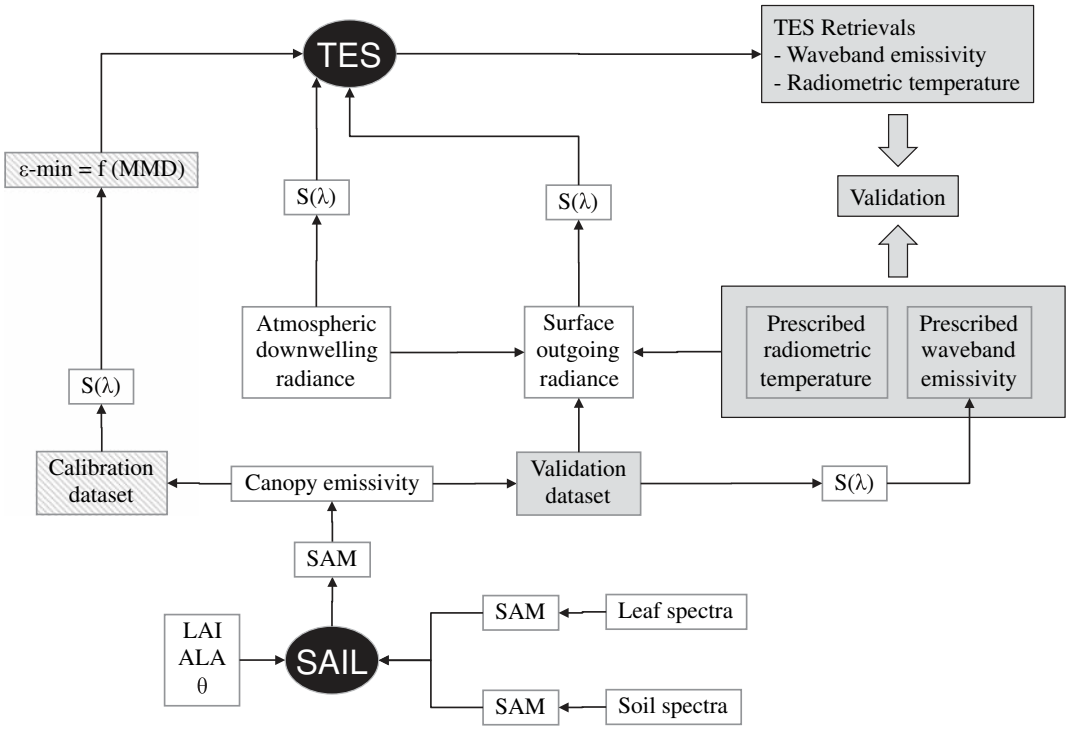

Fig. 1. Flowchart of the procedure we implemented to assess the TES performances over vegetation canopies. SAM was the algorithm used for filtering out the emissivity spectra that were similar. S (λ) stands for the calculation of waveband quantities. Others variables are defined in Sections 2 and 3. SAIL stands for SAIL-Thermique.

with an integrating sphere. All reflectance and transmittance values to be considered hereafter are directional-hemispherical quantities.

For soil samples, we used several spectral libraries, to be listed below. Since we focused on vegetation canopies, we excluded spectra collected over rock samples.

1. The ASTER spectral library version 2 was set up in the context of the EOS/ASTER mission (Baldridge et al., 2009). It included 41 reflectance spectra over the [0.4–14] μm spectral interval.
2. The MODIS University of California Santa Barbara (UCSB) spectral library was set up in the context of the EOS/MODIS mission (Zhang and Wan, 1999). It included 69 reflectance spectra over the [3–14] μm spectral interval.
3. The soil spectral library from the hydrologic atmospheric pilot experiment in the Sahel (HAPEX-Sahel) program included nine reflectance spectra over the [7–14] μm spectral interval (Nerry et al., 1996).
4. The soil spectral library collected in the context of the JORNada EXperiment (JORNEX) program included four reflectance spectra over the [2–14] μm spectral interval (Schmugge et al., 2002).
5. The soil spectral library of French Space Lab (ONERA) was set up using soil samples collected in southern France (Lesaignoux et al., 2013). It included 190 reflectance spectra over the [3–14] μm spectral interval, measured over 32 soil samples with five to seven soil moisture levels.

For leaf samples, we found one spectral library only. It was jointly acquired by the French Space Lab and the United States Geological Survey (USGS) Reston, VA, USA (Gerber et al., 2011). The spectral library included 64 spectra of leaf transmittance/reflectance over the [0.4–14] μm spectral interval, for 26 plant species at different leaf moisture levels.

Overall, 313 spectra of soil directional-hemispherical reflectance and 64 spectra of leaf directional-hemispherical transmittance/reflectance were available for conducting the SAIL-Thermique simulations. All spectra were resampled to the spectral resolution of the SAIL-Thermique simulations that is indicated in the next Section.

3.1.3. SAIL-Thermique simulations

To account for a wide range of soil and plant conditions, we considered large intervals of LAI and LIDF values (Table 1), by referring to Weiss and Baret (1999). In order to consider intermediate values for vegetation cover fraction between bare soil and full cover, we set LAI values between 0 (bare soil) and 7 (high vegetation cover), with narrower LAI intervals at low LAI values so that we accounted for the larger influence of LAI at these low values (Olioso, 1995). LIDF was computed by using an ellipsoidal function (Campbell, 1990), and we set the average leaf angle (ALA) between 15° and 75° in order to account for a wide range of leaf inclination conditions, i.e., from planophile to erectophile species (Weiss et al., 2004).

For the view zenith angle, we set the observation direction to nadir only. Indeed, former simulation studies showed that angular variation of canopy emissivity are low between nadir and 40° (Guillevic et al., 2003; Labed and Stoll, 1991; Olioso, 1995; Ren et al., 2015). The spectral interval and resolution of the SAIL-Thermique simulations were set to [7.5–13.5] μm and 10^{-3} μm, respectively. To consider a wide range of plant and soil conditions, we set up the simulations by mixing each spectrum for leaf and soil along with each LAI and ALA value.

3.1.4. Filtering of emissivity spectra and resulting database

To minimize redundancies in the library of simulated emissivity spectra, we filtered the SAIL-Thermique input and output spectra by removing those that depicted similarities in spectral behavior. We used the spectral angle mapper (SAM) algorithm that calculates

Table 1
SAIL-Thermique inputs used for the simulations.

Input parameter	Values
LAI	0, 0.25, 0.5, 1, 2, 4, 7
ALA	15°, 35°, 55°, 75°
View zenith angle	Nadir

the similarity between two spectra (Girouard et al., 2004). SAM measures the angle γ between two spectra, treating them as vectors in a v-dimensional space (v being the number of spectral values). We implemented the SAM procedure as following. Each spectrum was used as a reference and compared to the other ones. In case any of the latter was similar to the reference spectrum, it was removed from the library. Two spectra were considered similar when angle γ between both was lower than 1°.

The SAM based filtering was firstly applied to SAIL-Thermique input spectra. Among the 313 soil spectra and 64 leaf spectra to be filtered separately, SAM selected 65 spectra of soil reflectance/transmittance and 35 spectra of leaf reflectance. When combined with the LAI and ALA values, we simulated 63,700 canopy emissivity spectra (65 soil spectra × 35 leaf spectra × 7 LAI values × 4 ALA values) using SAIL-Thermique. The SAM based filtering was secondly applied to SAIL-Thermique output spectra, which led to the selection of 271 simulated emissivity spectra. The database of 271 emissivity spectra was split into two equal parts: a calibration data set with 136 spectra, and a validation dataset with 135 spectra.

3.2. Setting up a library of surface outgoing radiance to apply and validate TES

As explained in Section 2, TES is applied to TIR remote sensing measurements at the surface level, i.e. over a set of waveband values of surface outgoing radiance within the channels of the considered sensor. The surface outgoing radiance is the sum of the emission component that involves surface emissivity and radiometric temperature, and of the reflection component that involves atmospheric downwelling irradiance and surface reflectance, the latter being assumed equal to 1-emissivity (Schmugge et al., 1998).

We computed the emission component from the emissivity spectra and the prescribed values of surface radiometric temperature. We used the 135 emissivity spectra from the validation dataset. For each spectrum, 10 radiometric temperature values were randomly drawn (uniform distribution) within the [270–340] K range, with a maximum value of 305 K for LAI larger than 4, so that radiometric temperature is consistent with vegetation cover at satellite overpass around solar noon, for a large range of soil, plant and atmospheric conditions (Chávez et al., 2011).

We computed the reflection component from both emissivity spectra and spectra of atmospheric downwelling irradiance. We used the same emissivity spectra as selected when computing the emission component. We simulated the spectra of atmospheric downwelling irradiance using the MATISSE-V2 (Acronym for French label meaning "earth advance modeling for imagery and simulation of scenes and their environments") atmospheric radiative transfer model (Labarre et al., 2010; Labarre et al., 2011). We used atmospheric profiles from the Air Force Research Laboratory (AFRL) dataset (Simoneau et al., 2006) as inputs for MATISSE-V2. We selected three atmospheric profiles ("US standard 1976", "tropical" and "mid-latitude winter") that represented a large range of atmospheric conditions, from dry to humid atmospheres and from cold to warm atmospheres. The MATISSE simulations were conducted over the [740–1335] cm^{-1} spectral interval, with a 1 cm^{-1} spectral resolution that corresponds to 0.005 μm at 7.5 μm and to 0.02 μm at 13.5 μm. The spectra of atmospheric downwelling irradiance were then resampled to the spectral resolution of the SAIL-Thermique simulations, by using a linear interpolation.

We combined each of the 135 emissivity spectra from the validation dataset with the 10 prescribed values of radiometric temperature and the three spectra of atmospheric downwelling irradiance. Among the resulting 4050 spectra of surface outgoing radiance, we selected those for which the surface - air temperature gradient ranged between −10 K and +30 K, where air temperature is the temperature value at the first atmospheric profile level (Du et al., 2015; Sobrino and Romaguera, 2004). The goal was to select realistic surface – air temperature gradients for a large range of soil, plant and atmospheric conditions. The final dataset subsequently included 2157 spectra of surface outgoing radiance.

3.3. Computing waveband emissivity and radiances from simulated spectra

Calibrating and applying TES requires accounting for the sensor spectral configuration. We considered those of three existing sensors: ASTER (Yamaguchi et al., 1998), MODIS (Justice et al., 1998) and MASTER (Hook et al., 2001). We also considered the spectral configurations of two sensors under study: HyspIRI (Green et al., 2012) and MISTIGRI (Lagouarde et al., 2013). Overall, considering a panel of different sensors permitted to address the impact of channel number on the TES performances, where TES aims to capture the emissivity spectral contrast from multispectral observations.

The characteristics of the channel filters are given in Fig. 2. They were obtained from dedicated web sites for ASTER (https://asterweb.jpl.nasa.gov/characteristics.asp), TERRA/MODIS (ftp://mcst.ssaihq.com/permanent/MCST/PFM_L1B_LUT_4-30-99/L1B_RSR_LUT/) and MASTER (https://asapdata.arc.nasa.gov/Master/srf/May_01/). The spectral configurations of MODIS, ASTER and MASTER included three, five and 10 channels, respectively. Although including MASTER band 41 @ 7.85 μm was questionable because of atmospheric perturbations, we included all the MASTER channels since it permitted to address a configuration with a large number of channels. At the time of the study, the design of the HyspIRI and MISTIGRI spectral configurations were in progress, and we set up their configurations according to the available information. By following Hulley (2011), we considered the five ASTER channels along with the MODIS channel located at 12 μm for HyspIRI. For MISTIGRI, we followed the specifications from the A-phase of the MISTIGRI mission (Lagouarde et al., 2013), and we set-up two configurations: one with three channels and the other one with four channels. The corresponding channel filters were provided by the French space agency (CNES). For MISTIGRI, larger bandwidths aimed to reduce instrumental noise induced by the use of micro-bolometer detectors (Lagouarde et al., 2013).

The channel filters were interpolated to the spectral resolution of the SAIL-Thermique simulations (10^{-3} μm). Finally, we computed the waveband quantities in each channel by convolving the spectra (e.g., emissivity, surface outgoing radiance and atmospheric downwelling irradiance) with the corresponding filter.

3.4. Calibrating and validating the TES method

The ε-min - MMD empirical relationship of the TES method was calibrated for each sensor spectral configuration. We used the waveband values derived from the 136 emissivity spectra of the calibration dataset. Coefficients A, B and C were calibrated over the dataset of (ε-min, MMD) pairs, by minimizing the quadratic difference between actual and predicted values. We used the R "Optim" function that relies on the Newton's method (R Development Core Team, 2011), and we obtained the same calibration results regardless of initial guess. The resulting root mean square error (RMSE) was calculated as the calibration residual error. Additionally, we evaluated the calibrated ε-min - MMD relationship against the 135 emissivity spectra from the validation dataset.

For each sensor spectral configuration, we used the calibrated coefficients to apply TES over the waveband values of surface outgoing radiance along with the waveband values of atmospheric downwelling irradiance. Then, TES retrievals of waveband emissivity and radiometric temperature were compared against the original prescriptions used to calculate surface outgoing radiance (Section 3.2). The quadratic differences were expressed in terms of RMSE values.

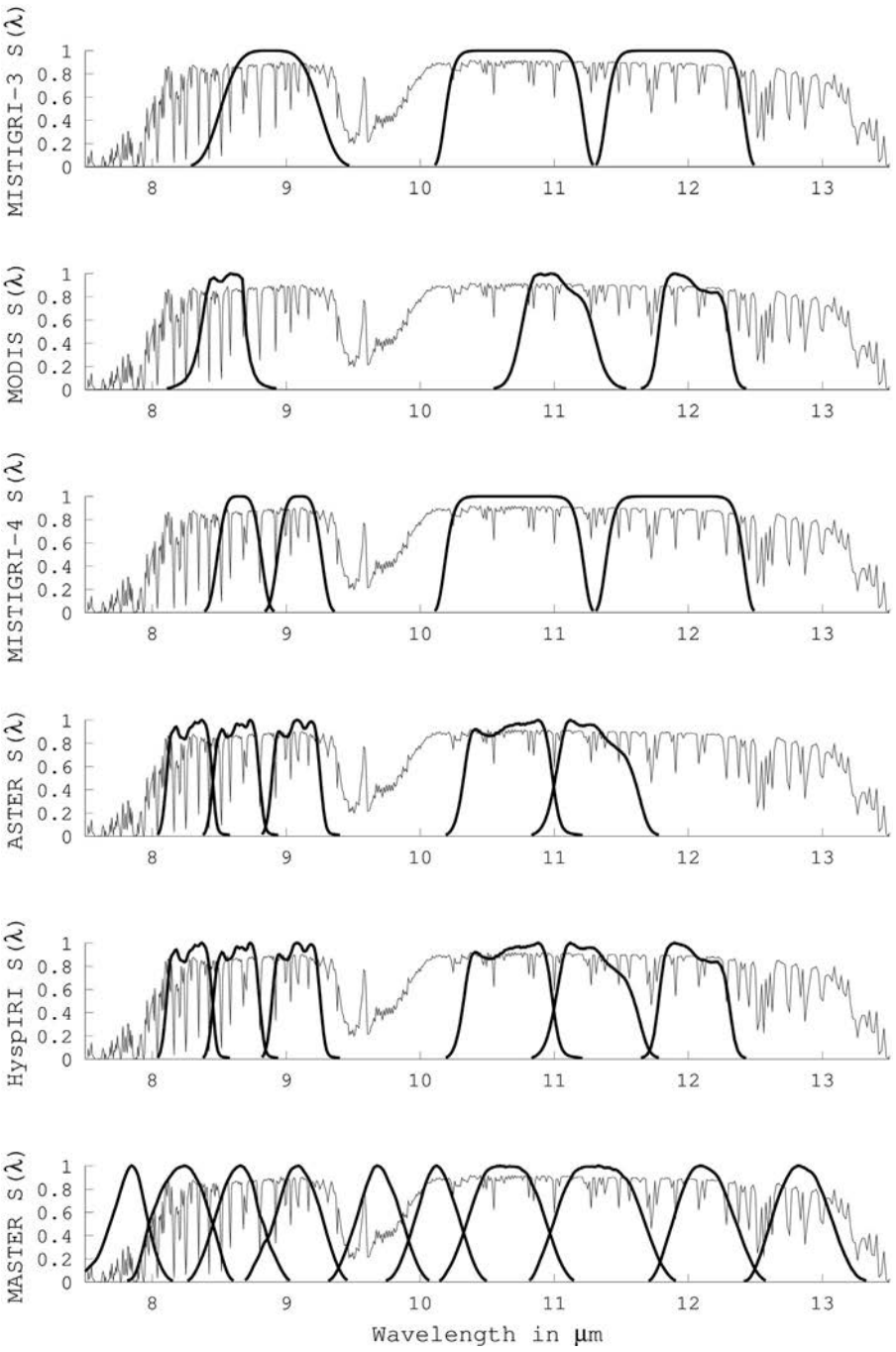

Fig. 2. Characteristics of the spectral configuration for each of the sensors we considered (black lines), along with a typical example of atmospheric transmittance (gray lines). MISTIGRI-N stands for the MISTIGRI configurations that involve N channels. The configurations are ranked according to a growing number of channels.

4. Results

We first report the results obtained when calibrating the ε-min - MMD relationship (Section 4.1), and when validating the TES retrievals of emissivity and radiometric temperature (Section 4.2). We then compare the SAIL-Thermique based results for TES calibration/validation against those reported in former studies that relied on single or linearly mixed samples of soil/leaf spectra (Section 4.3).

4.1. Calibration of the TES empirical relationship

Fig. 3 displays a typical example of the calibration results for the ε-min - MMD relationship when considering the MASTER sensor. We obtained similar results with the other sensor spectral configurations. Indeed, the calibrated relationships were rather similar for low MMD values, with differences in ε-min value around 0.007 for a MMD value of 0.1, and they could be quite different for large emissivity spectral contrasts, with differences in ε-min value up to 0.02 for MMD values of 0.3. Also, the channel number impacted the MMD range, up to 0.05 MMD units for large MMD values.

Table 2 displays the results we obtained when calibrating the ε-min - MMD relationship for each sensor spectral configuration, as well as when comparing the ε-min estimates against those derived from the validation dataset. The A, B, C coefficients were different from one configuration to another, but they were similar when channel numbers were close (e.g., MODIS versus MISTIGRI with 3 channels, ASTER versus MISTIGRI with 4 channels, or ASTER versus HyspIRI). The calibration errors decreased by 25–30% when the channel number increased from 3

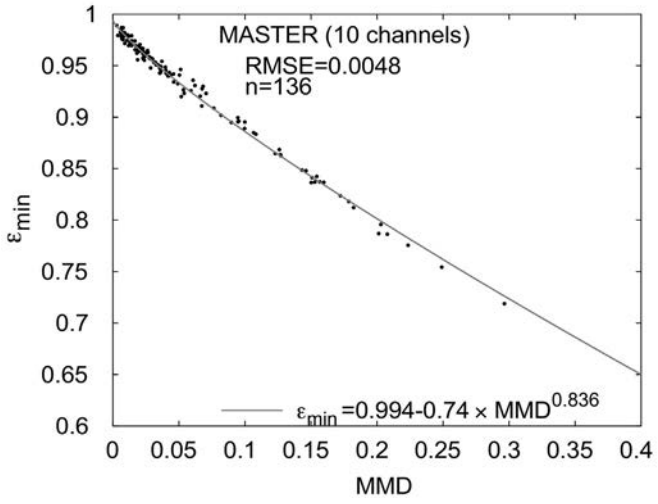

Fig. 3. Calibration of the ε-min - MMD relationship for the spectral configuration of the MASTER sensor. Dots correspond to the samples used for the calibration, and continuous line is the calibrated relation. The RMSE value indicates the calibration residual error. The n value indicates the sampling number.

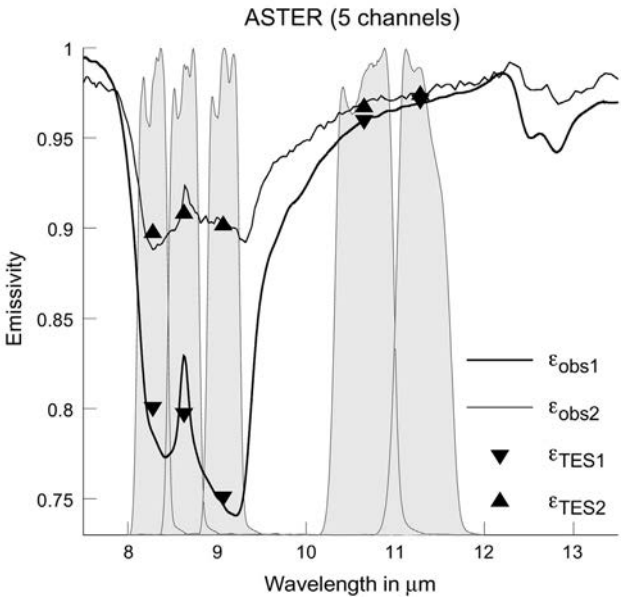

Fig. 4. Comparison of TES retrievals of waveband emissivity (labeled ε_{TES1} and ε_{TES2}) against reference emissivity spectra (labeled ε_{obs1} and ε_{obs2}) when considering two typical emissivity spectra from the validation dataset simulated with SAIL-Thermique. The results are given for the ASTER spectral configuration. Gray areas indicate the ASTER channel filters.

to 10, and it remained lower than 0.0065. Similar results were obtained when comparing ε-min estimates against those derived from the validation dataset, with errors lower than 0.007.

4.2. Validation of the TES retrievals of emissivity and radiometric temperature

Fig. 4 displays a typical example of the results obtained when comparing TES retrievals of waveband emissivity against prescribed values from the validation dataset. Prescribed values were waveband emissivities derived from the emissivity spectra used to compute waveband surface outgoing radiance over which was apply TES (see Fig. 1). This typical example corresponded to the ASTER spectral configuration, and we obtained similar results with the other sensor spectral configurations. It is shown that the emissivity spectra were well retrieved by TES. For a given spectrum, the retrievals of waveband emissivity were closer to the prescribed values at larger wavelengths that usually corresponded to flatter portions of the emissivity spectra (10 to 12 μm).

Fig. 5 displays the comparison of the TES retrievals of waveband emissivity against the prescribed values derived from reference spectra of the validation dataset, when considering the MISTIGRI spectral configuration with four channels. We obtained similar results with the other sensors. Regardless of channel, we noted larger discrepancies around the 1:1 line for large emissivity values. Besides, retrievals of waveband emissivity agreed better with prescribed values for larger wavelengths (10 to 12 μm) that corresponded to flatter portions of emissivity spectra (Fig. 4). This was observed for all sensor spectral configurations, with RMSE values decreasing from 0.01 to 0.005, apart from the MASTER channel at 7.8 μm (Fig. 6).

Fig. 7 displays the comparison of TES retrievals of radiometric temperature against the prescribed values when considering HyspIRI. We obtained similar results with the other sensors, with RMSE values of 0.47 K for MISTIGRI with 3 channels, 0.44 K for MODIS, 0.38 K for MISTIGRI with 4 channels, 0.35 K for ASTER, 0.34 K for HyspIRI, and 0.28 K for MASTER. The results were consistent with those obtained when validating emissivity retrievals: we noted better agreements between retrieved and prescribed values of radiometric temperature for sensors with more channels, the RMSE value being twice lower when using 10 channels rather than 3.

Table 2
Results of the ε-min - MMD relationship calibration ($\varepsilon\text{-min} = A + B \times MMD^C$) for each of the six sensors we considered. The results are ranked according to a growing number of channels. Calibration dataset included 136 emissivity spectra, and validation dataset included 135 emissivity spectra.

Sensor	Number of channels	Calibrated coefficients			RMSE (calibration dataset)	RMSE (validation dataset)
		A	B	C		
MISTIGRI	3	0.987	−0.688	0.821	0.0065	0.0069
MODIS	3	0.989	−0.674	0.815	0.0064	0.0065
MISTIGRI	4	0.987	−0.722	0.850	0.0056	0.0057
ASTER	5	0.989	−0.737	0.834	0.0055	0.0052
HyspIRI	6	0.989	−0.738	0.860	0.0052	0.0051
MASTER	10	0.994	−0.740	0.836	0.0048	0.0049

4.3. Impact of cavity effect on TES calibration and retrievals

For the spectral configurations of ASTER and MODIS, we compared our TES calibration/validation results against those reported in former studies (Gillespie et al., 1998; Hulley et al., 2012a; Jimenez-Munoz et al., 2014). We could not compare the calibrated coefficients for MASTER and HyspIRI, because of differences in channel selections (Grigsby et al., 2015; Hulley, 2011).

Table 3 displays the various coefficients of the ε-min - MMD relationship proposed for MODIS and ASTER by the current study and by former studies. The resulting ε-min estimates differed by 0.015 on average, and up to 0.025 for MMD larger than 0.1. Further, the ε-min predictions derived from our calibration were systematically larger than those derived from former calibrations. As an example, Fig. 8 displays the ε-min - MMD relationship when considering the newly fitted calibration we proposed in the current study and that proposed by Gillespie et al. (1998) for the ASTER spectral configuration. We obtained similar results when dealing with MODIS. Fig. 8 shows that both calibrations provided different ε-min predictions, and that the ε-min predictions derived from our calibration were systematically larger than those derived from the Gillespie's calibration, mostly for intermediate MMD values. The bias between predictions and actual values from our calibration dataset was obviously close to zero for our calibration, while it was about

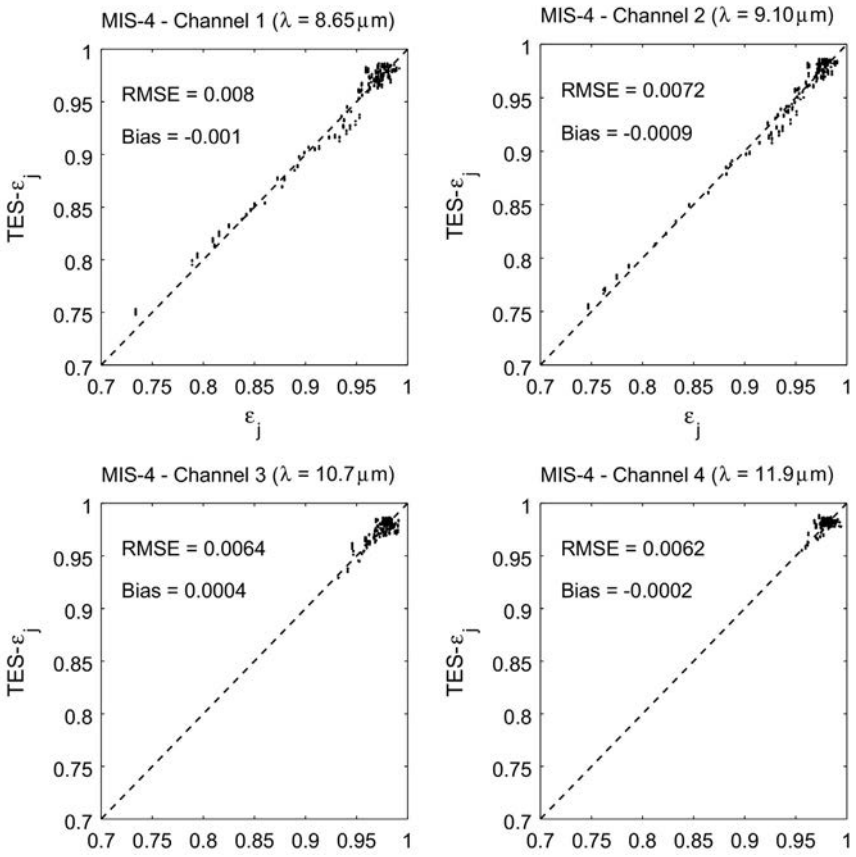

Fig. 5. Comparison of TES retrievals of waveband emissivity against waveband values derived from our validation dataset of emissivity spectra. The results are given for the MISTIGRI spectral configuration that included four channels. Dashed line is the 1:1 line.

0.006 for the Gillespie's one. As compared to the residual error we obtained with our calibration (RMSE value of 0.0055, Table 2), the quadratic difference between actual values from our calibration dataset and predictions from the Gillespie's calibration was twice larger (RMSE of 0.0095).

We quantified the impact of differences in ε-min predictions by comparing the Gillespie's calibration for ASTER against our validation dataset. The comparisons of TES retrievals against prescribed values are displayed in Figs. 9 and 10. It is shown that lower estimates of ε-min induced (1) lower estimates of waveband emissivity for all ASTER channels, with bias values ranging from 0.007 to 0.009, and (2) larger estimates of radiometric temperature, of about 0.4 K. Resulting errors on waveband emissivity and radiometric temperature were almost twice larger than those obtained when validating our calibration. Indeed, RMSE ranged from 0.011 to 0.015 for emissivity and it was 0.6 K for radiometric temperature with the Gillespie's calibration (Figs. 9 and 10), to be compared to RMSE ranging from 0.005 to 0.008 for emissivity and RMSE of 0.35 K for radiometric temperature with our calibration (Fig. 6 and Section 4.2).

We finally quantified the impact of cavity effect by comparing the calibration obtained from SAIL-Thermique simulations against that obtained if selecting soil and leaf spectra only. In order to minimize other driver effects and to focus on cavity effect, we selected only the soil and leaf spectra involved in the SAIL-Thermique simulations. Soil emissivity ε_s was assumed equal to absorptance, and computed from reflectance ϱ_s (i.e., $\varepsilon_s = 1 - \varrho_s$). Leaf emissivity ε_l was assumed equal to absorptance, and computed from leaf reflectance ϱ_l and transmittance τ_l ($\varepsilon_l = 1 - \varrho_l - \tau_l$). The results are displayed in Fig. 11. It is shown that the calibration from soil and leaf spectra only provided lower ε-min estimates as compared to the calibration from SAIL-Thermique simulations. The bias was similar to that obtained with the Gillespie's calibration (Fig. 8), with a slightly lower value (0.004 versus 0.0055). The lowest ε-min estimates were observed for intermediate MMD values that correspond to intermediate vegetation cover.

5. Discussion

The calibration/validation results for emissivity and temperature retrievals were good. This underlines the relevance of the TES empirical relationship, especially when (1) using emissivity spectra simulations that account for radiative transfer within the canopy with subsequent cavity effect and (2) considering a range of soil and plant conditions, from bare soil to full vegetation cover. However, the absolute RMSE values found in this study should be considered with caution for two reasons. First, we addressed the land surface level without any consideration of atmospheric or instrumental perturbations. Second, the calibration and validation datasets were not fully independent since they were derived from the same model, which partly explains the similar RMSE values we observed for calibration and validation.

The calibration/validation results were better for sensor spectral configurations with more channels that permitted to capture emissivity spectral contrast more efficiently, which is in agreement with previous studies. For a given spectral configuration, emissivity retrievals were worse at lower wavelengths, because of sharp changes in emissivity between 8 and 10 μm, as compared to flatter spectra portions between 10 and 12 μm (Fig. 4). The worst emissivity retrievals for the MASTER channel located at 7.8 μm was ascribed to large atmospheric irradiance below 8 μm. Thus, it may be better excluding this channel, even at the ground level, although TES retrievals of radiometric temperature were good. Apart from channels below 8 μm, obtaining better accuracies on

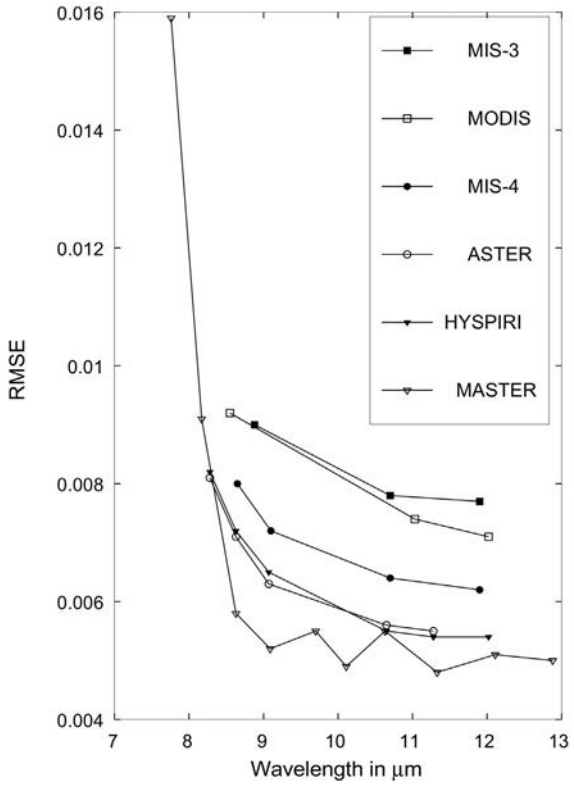

Fig. 6. Averaged RMSE values obtained for each sensor channel when comparing TES retrievals of emissivity against waveband values derived from our validation dataset of emissivity spectra. MIS-N stands for the spectral configurations of the MISTIGRI sensor with N channels.

emissivity retrievals at lower wavelengths may require finer channels to capture sharp changes in emissivity. However, this issue must be addressed by accounting for atmospheric and instrumental perturbations that may affect the signal quality in a larger extent with finer channels. Finally, the observed discrepancies around the 1:1 line for large emissivity values (Figs. 5 and 9) were ascribed to the gray body problem. The latter corresponds to low retrieval performances for TES over land

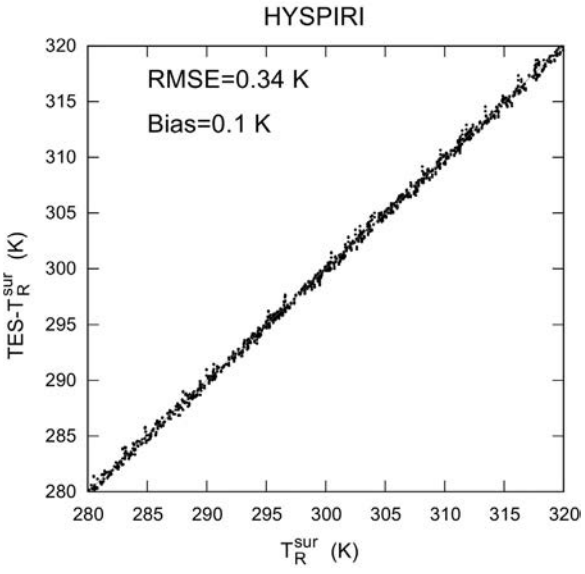

Fig. 7. Comparison of TES retrievals of radiometric temperature against prescribed values. The results are given for the HyspIRI spectral configuration that included six channels.

Table 3
Existing calibrations for the ε-min - MMD relationship, displayed as values of the coefficients A, B and C, when dealing with the MODIS and ASTER sensors. Last column indicates the corresponding literature references.

Sensor	Number of channels	Calibrated coefficients			Reference
		A	B	C	
MODIS	3	0.985	−0.750	0.832	(Hulley et al., 2012a)
MODIS	3	0.998	−0.654	0.736	(Jimenez-Munoz et al., 2014)
MODIS	3	0.989	−0.674	0.815	The current study
ASTER	5	0.994	−0.687	0.737	(Gillespie et al., 1998)
ASTER	5	0.989	−0.737	0.834	The current study

surfaces that depicted low emissivity spectral contrasts, usually for large vegetation covers (Coll et al., 2007; Jacob et al., 2004; Ogawa et al., 2008).

For the ASTER and MODIS spectral configurations, it was shown that ε-min estimates from our calibration were systematically larger than ε-min estimates from former calibrations, especially for intermediate MMD values that mostly corresponded to intermediate vegetation covers. The resulting differences on emissivity and radiometric temperature retrievals could reach up to 0.025 (0.015 on average, Fig. 9) and 2 K (0.6 K on average, Fig. 10). The larger ε-min estimates obtained with our calibrations were due to the difference in the samples used to fit the ε-min - MMD relationship. First, we excluded soil spectra corresponding to mineral samples that tended to shift downward the ε-min - MMD relationship, as shown by Schmugge et al. (1998). Second, our calibration dataset included more vegetation surfaces as compared to former studies, since we focused on plant canopies with LAI between 0 and 7. Third, introducing spectra with cavity effect tended to shift upward the ε-min - MMD relationship (Anton and Ross, 1990; Chen et al., 2004; Merlin and Chehbouni, 2004; Olioso, 1995). This was confirmed when comparing the calibration from SAIL-Thermique simulations against that from soil and leaf spectra only (Fig. 11).

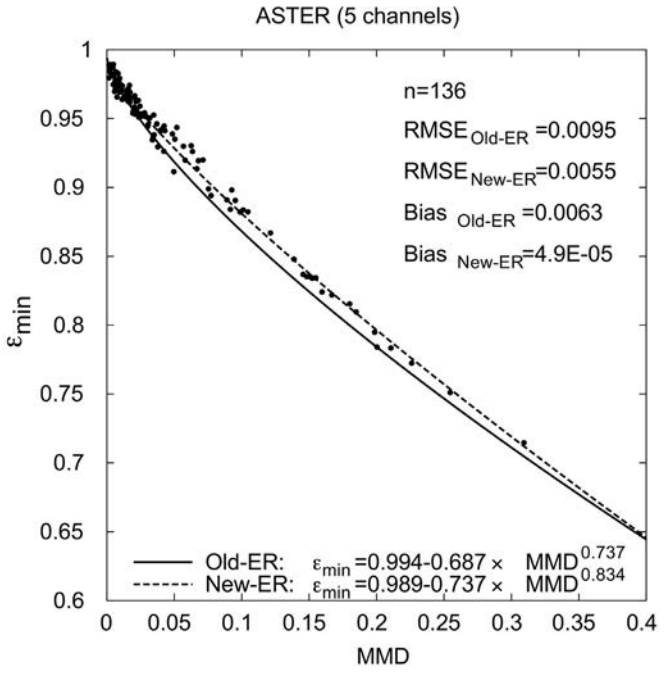

Fig. 8. Comparison between the calibration obtained in the current study with SAIL-Thermique simulations for ASTER (labeled New-ER for new fitting of empirical relationship) and that proposed by Gillespie et al. (1998) for the same sensor (labeled Old-ER for old empirical relationship). Scatterplots are the (ε-min, MMD) pairs we used the in current study.

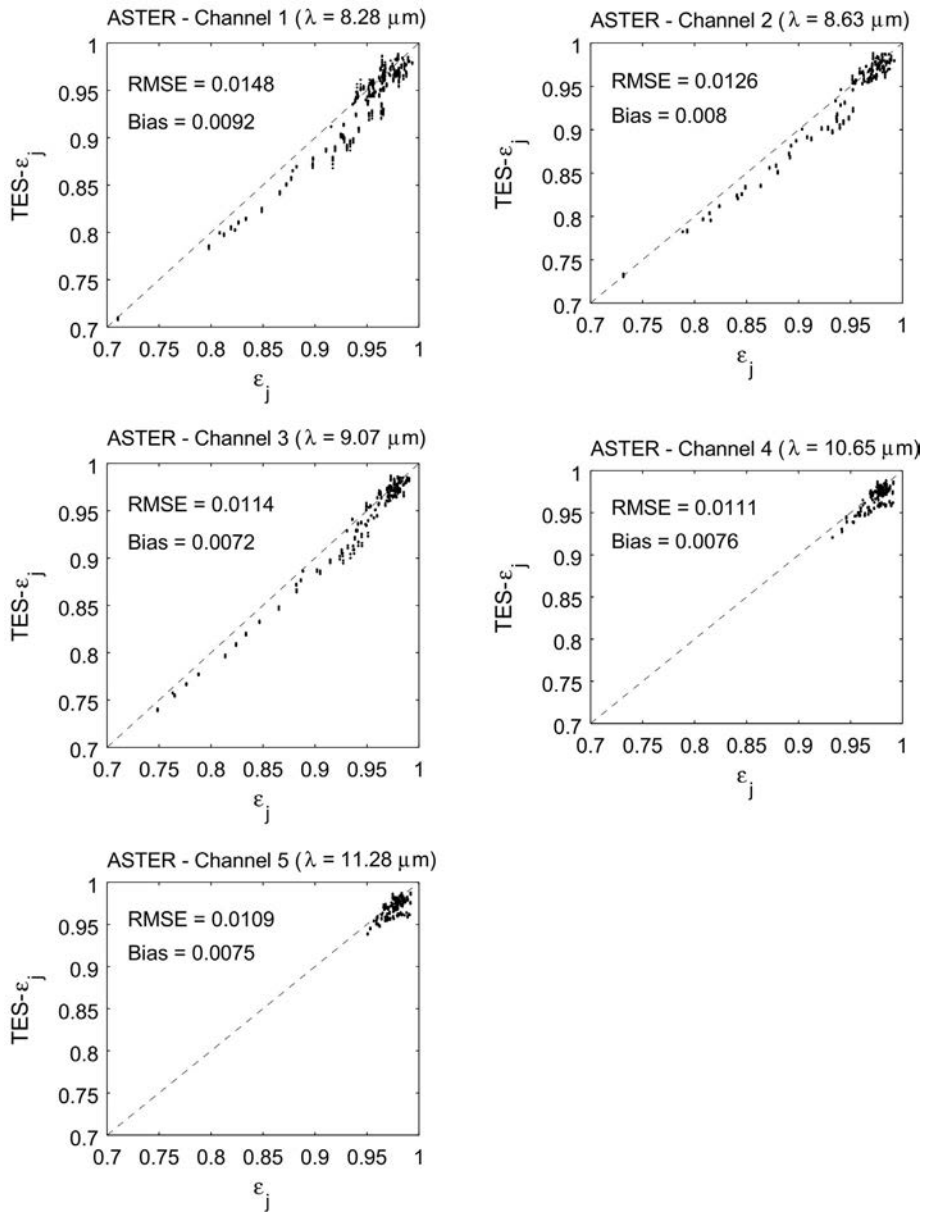

Fig. 9. Comparison of waveband emissivity retrieved with TES when using the calibration proposed by Gillespie et al. (1998) for ASTER against waveband values derived from our validation dataset of emissivity spectra. Dashed line is the 1:1 line.

Former calibration results were different from one study to another (Section 2). Differences were also observed in the current study that relied on a new type of spectral library, where the latter accounted for cavity effect while including a wide range of soil and plant conditions. Overall, the variability we observed on calibration results questioned the relevance and representativeness of any dataset to be used for calibration, and it underlined how the choice of the spectral library is a crucial step. An appropriate set up would require accounting for sample occurrences at the worldwide scale.

The use of a radiative transfer model for the calibration of the ε-min - MMD relationship permitted to account for radiative transfer within vegetation canopy and subsequent cavity effect while considering a wide range of soil and plant conditions. This gave us the opportunity to study the variation of the (ε-min - MMD) pairs as a function of the vegetation cover. Fig. 12 displays changes in canopy emissivity spectra as LAI increases for a given set of soil and leaf spectra (top), along with the resulting changes in (ε-min - MMD) pairs (bottom). It is shown that emissivity spectra become flat with values closer to unity as LAI increases, as empirically reported by Neinavaz et al. (2016a), which induces a displacement of the (ε-min - MMD) pairs along the ε-min - MMD empirical relationship. Thus, increasing LAI with SAIL-Thermique induced similar trends than using single or linearly mixed samples of soil/leaf spectra, i.e. the displacement of the (ε-min - MMD) pairs along the empirical relationship. This is explained by the underlying TES assumption, where any change in ε-min induces change in MMD because ε-max is bounded on [0.98–1].

6. Concluding remarks

The current study focused on evaluating the TES performances over various vegetation canopies, from bare soil to full vegetation cover. This research is based on the use of the SAIL radiative transfer model to account for cavity effect within vegetation canopy. As compared to previous studies based on the use of leaf and soil spectra only, differences

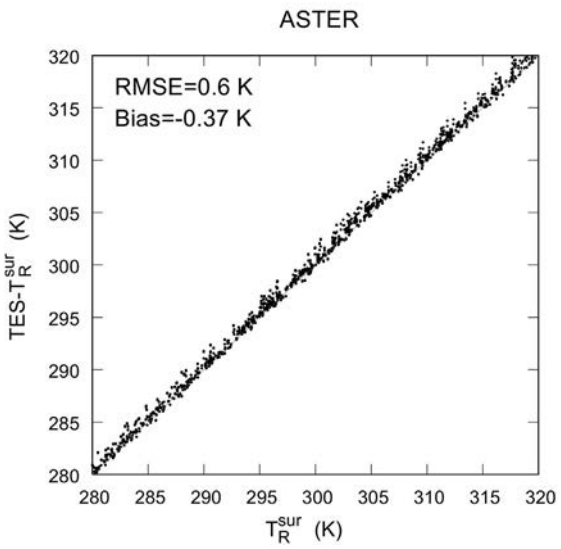

Fig. 10. Comparison of radiometric temperature retrieved with TES when using the calibration proposed by Gillespie et al. (1998) for ASTER against the prescribed values.

occurred mainly for intermediate vegetation cover, with non-negligible consequences on the TES retrievals of emissivity and radiometric temperature. This raises the question of the representativeness of the calibration dataset, in relation to the considered type of land surface. To a lesser extent, the TES performances were in agreement with those reported in former studies: retrieval performances are better when considering more channels, the emissivity is better estimated for spectral intervals with flatter emissivity spectra, and it is less well estimated for large emissivity values because of the gray body problem.

The current study relied on a synthetic dataset. Although comparative results permitted to underline the impact of cavity effect for a large range of soil and plant conditions, it is necessary to confront these outcomes against ground-based measurements, given (1) measurement methods were recently proposed for reflectance spectra (Neinavaz et al., 2016a; Neinavaz et al., 2016b; Rock et al., 2016) and (2) multispectral measurements have been conducted over large spectral bands (Olioso et al., 2014; Olioso et al., 2007). Besides, the current study focused on land surface level, without any consideration of instrumental and atmospheric perturbations, whereas the latter can have significant consequences (e.g., Hulley et al., 2012b; Jacob et al., 2004). In the context of forthcoming space missions such as HyspIRI (Green et al., 2012), MISTIGRI (Lagouarde et al., 2013), or THIRSTY (Crebassol et al., 2014), ongoing investigations address the combined effects of emissivity spectral contrast, spectral variations of atmospheric perturbations, and instrumental effects that depend upon bandwidths. Thus, a preliminary study suggested to merge the two MISTIGRI channels at 8.6 and 9.1 μm, in order to reduce the instrumental noise induced by the use of micro-bolometer detectors (Lagouarde et al., 2013).

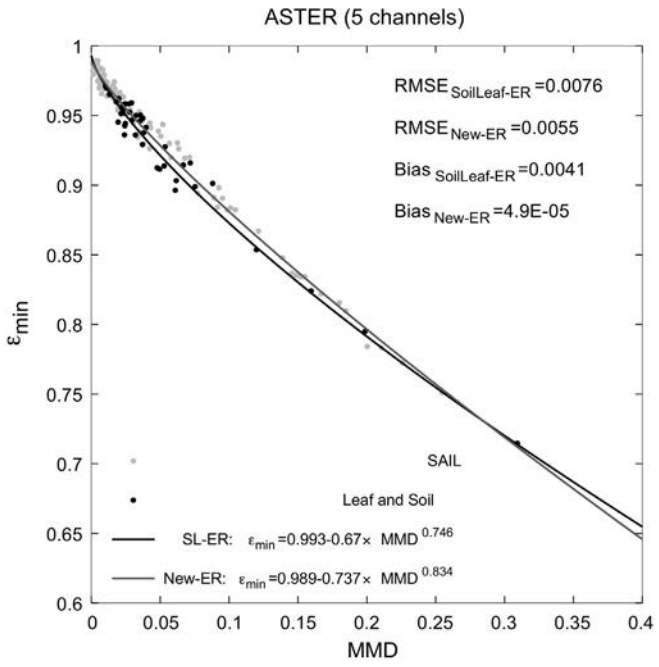

Fig. 11. Comparison between the calibration obtained in the current study with SAIL-Thermique simulations (labeled New-ER for new fitting of empirical relationship) and that obtained if selecting soil and leaf spectra only (labeled SL-ER). Scatterplots are the (ε-min, MMD) pairs used for the calibrations, in black for soil and leaf spectra only, and in gray for the SAIL-Thermique simulations. The results are given for the ASTER spectral configuration.

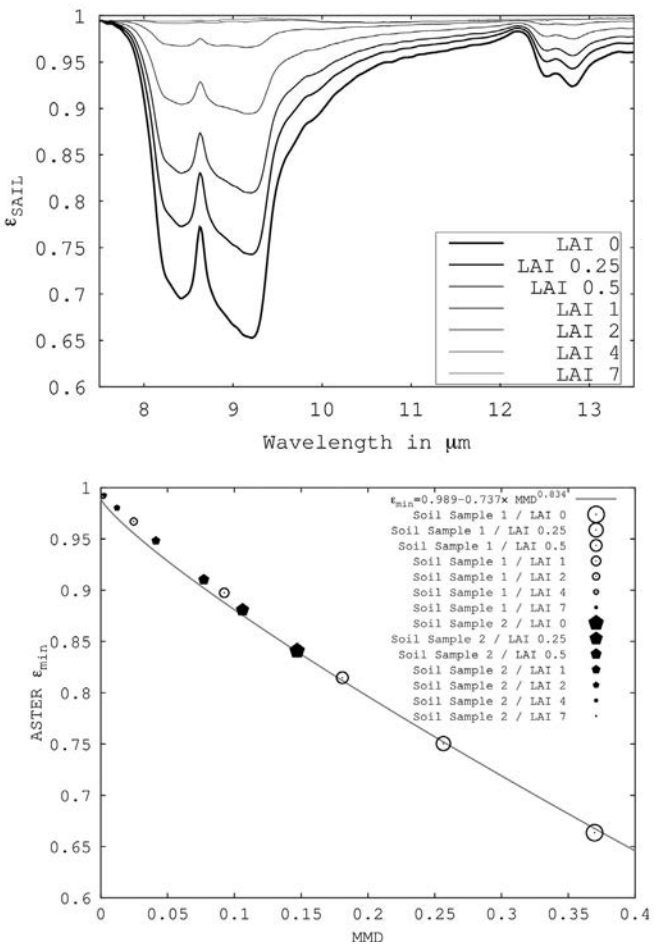

Fig. 12. (Top) Change in emissivity spectra as simulated with SAIL-Thermique for increasing LAI. (Bottom) Change in (ε-min, MMD) pairs as simulated with SAIL-Thermique when LAI increases. Results are given for the ASTER spectral configuration. The continuous line is the empirical relationship calibration we obtained when using our simulated dataset.

Acknowledgments

Financial grants come from French Space Agency (contracts CNES 104075). We thank Philippe Gamet (CNES Toulouse, France) for providing the prototypes of the MISTIGRI channel filters. We are grateful to Luc Labarre (ONERA/DOTA, Palaiseau, France) for his help in the implementation of the MATISSE code.

References

Anderson, M.C., Allen, R.G., Morse, A., Kustas, W.P., 2012. Use of Landsat thermal imagery in monitoring evapotranspiration and managing water resources. Remote Sens. Environ. 122, 50–65.

Anton, Y.A., Ross, Y.K., 1990. Emissivity of a vegetation-soil system. Sov. J. Remote. Sens. 7, 859–869 (in English translation).

Baldridge, A., Hook, S., Grove, C., Rivera, G., 2009. The ASTER spectral library version 2.0. Remote Sens. Environ. 113, 711–715.

Barducci, A., Pippi, I., 1996. Temperature and emissivity retrieval from remotely sensed images using the "grey body emissivity" method. IEEE Trans. Geosci. Remote Sens. 34, 681–695.

Campbell, G.S., 1990. Derivation of an angle density function for canopies with ellipsoidal leaf angle distributions. Agric. For. Meteorol. 49, 173–176.

Chávez, J., Gowda, P., Howell, T., Garcia, L., Copeland, K., Neale, C., 2011. ET mapping with high-resolution airborne remote sensing data in an advective semiarid environment. J. Irrig. Drain. Eng. 138, 416–423.

Chehbouni, A., Hoedjes, J.C.B., Rodriquez, J.-C., Watts, C.J., Garatuza, J., Jacob, F., Kerr, Y.H., 2008. Using remotely sensed data to estimate area-averaged daily surface fluxes over a semi-arid mixed agricultural land. Agric. For. Meteorol. 148, 330–342.

Chen, L.F., Li, Z.L., Liu, Q.H., Chen, S., Tang, Y., Zhong, B., 2004. Definition of component effective emissivity for heterogeneous and non-isothermal surfaces and its approximate calculation. Int. J. Remote Sens. 25, 231–244.

Coll, C., Caselles, V., Rubio, E., Valor, E., Sospedra, F., Baret, F., Prévot, L., Jacob, F., 2002. Temperature and emissivity extracted from airborne multi-channel data in the ReSeDA experiment. Agronomie 22, 567–573.

Coll, C., Valor, E., Caselles, V., Niclòs, R., 2003. Adjusted normalized emissivity method for surface temperature and emissivity retrieval from optical and thermal infrared remote sensing data. J. Geophys. Res.-Atmos. 108 (n/a-n/a).

Coll, C., Caselles, V., Valor, E., Niclòs, R., Sánchez, J.M., Galve, J.M., Mira, M., 2007. Temperature and emissivity separation from ASTER data for low spectral contrast surfaces. Remote Sens. Environ. 110, 162–175.

Courault, D., Jacob, F., Benoit, V., Weiss, M., Marloie, O., Hanocq, J.F., Fillol, E., Olioso, A., Dedieu, G., Gouaux, P., Gay, M., French, A., 2009. Influence of agricultural practices on micrometerological spatial variations at local and regional scales. Int. J. Remote Sens. 30, 1183–1205.

Crebassol, P., Lgouarde, J.P., Hook, S., 2014. Thirsty thermal infrared spatial system. Geoscience and Remote Sensing Symposium (IGARSS), 2014 IEEE International, pp. 3021–3024.

Dash, P., Göttsche, F.M., Olesen, F.S., Fischer, H., 2002. Land surface temperature and emissivity estimation from passive sensor data: theory and practice-current trends. Int. J. Remote Sens. 23, 2563–2594.

Du, C., Ren, H., Qin, Q., Meng, J., Zhao, S., 2015. A practical split-window algorithm for estimating land surface temperature from Landsat 8 data. Remote Sens. 7, 647.

Er-Raki, S., Chehbouni, A., Hoedjes, J., Ezzahar, J., Duchemin, B., Jacob, F., 2008. Improvement of FAO-56 method for olive orchards through sequential assimilation of thermal infrared-based estimates of ET. Agric. Water Manag. 95, 309–321.

Francois, C., Ottle, C., Prevot, L., 1997. Analytical parameterization of canopy directional emissivity and directional radiance in the thermal infrared. Application on the retrieval of soil and foliage temperatures using two directional measurements. Int. J. Remote Sens. 18, 2587–2621.

French, A., Schmugge, T., Ritchie, J., Hsu, A., Jacob, F., Ogawa, K., 2008. Detecting land cover change at the Jornada Experimental Range, New Mexico with ASTER emissivities. Remote Sens. Environ. 112, 1730–1748.

Galleguillos, M., Jacob, F., Prevot, L., Lagacherie, P., Shunlin, L., 2011. Mapping daily evapotranspiration over a Mediterranean vineyard watershed. IEEE Geosci. Remote Sens. Lett. 8, 168–172.

Gerber, F., Marion, R., Olioso, A., Jacquemoud, S., Ribeiro da Luz, B., Fabre, S., 2011. Modeling directional–hemispherical reflectance and transmittance of fresh and dry leaves from 0.4 μm to 5.7 μm with the PROSPECT-VISIR model. Remote Sens. Environ. 115, 404–414.

Gillespie, A., Rokugawa, S., Matsunaga, T., Cothern, J.S., Hook, S., Kahle, A.B., 1998. A temperature and emissivity separation algorithm for advanced spaceborne thermal emission and reflection radiometer (ASTER) images. IEEE Trans. Geosci. Remote Sens. 36, 1113–1126.

Gillespie, A.R., Abbott, E.A., Gilson, L., Hulley, G., Jiménez-Muñoz, J.-C., Sobrino, J.A., 2011. Residual errors in ASTER temperature and emissivity standard products AST08 and AST05. Remote Sens. Environ. 115, 3681–3694.

Girouard, G., Bannari, A., El Harti, A., Desrochers, A., 2004. Validated spectral angle mapper algorithm for geological mapping: comparative study between QuickBird and Landsat-TM. XXth ISPRS Congress, Geo-Imagery Bridging Continents, Istanbul, Turkey, pp. 12–23.

Göttsche, F.-M., Hulley, G.C., 2012. Validation of six satellite-retrieved land surface emissivity products over two land cover types in a hyper-arid region. Remote Sens. Environ. 124, 149–158.

Green, R.O., Hook, S.J., Middleton, E., Turner, W., Ungar, S., Knox, R., 2012. The HyspIRI Decadal Survey Mission: Update on the Mission Concept and Science Objectives for Global Imaging Spectroscopy and Multi-spectral Thermal Measurements.

van de Griend, A.A., Owe, M., 1993. On the relationship between thermal emissivity and the normalized difference vegetation index for natural surfaces. Int. J. Remote Sens. 14, 1119–1131.

Grigsby, S.P., Hulley, G.C., Roberts, D.A., Scheele, C., Ustin, S.L., Alsina, M.M., 2015. Improved surface temperature estimates with MASTER/AVIRIS sensor fusion. Remote Sens. Environ. 167, 53–63.

Guillevic, P., Gastellu-Etchegorry, J.P., Demarty, J., Prévot, L., 2003. Thermal infrared radiative transfer within three-dimensional vegetation covers. J. Geophys. Res.-Atmos. 108, 4248.

Hook, S.J., Myers, J.J., Thome, K.J., Fitzgerald, M., Kahle, A.B., 2001. The MODIS/ASTER airborne simulator (MASTER) — a new instrument for earth science studies. Remote Sens. Environ. 76, 93–102.

Hulley, G., 2011. HyspIRI Level-2 Thermal Infrared (TIR) Land Surface Temperature and Emissivity Algorithm Theoretical Basis Document. Jet Propulsion Laboratory, National Aeronautics and Space Administration, Pasadena, CA.

Hulley, G.C., Hook, S.J., 2011. Generating consistent land surface temperature and emissivity products between ASTER and MODIS data for earth science research. IEEE Trans. Geosci. Remote Sens. 49, 1304–1315.

Hulley, G.C., Hook, S.J., Hughes, C., 2012a. MODIS MOD21 land surface temperature and emissivity algorithm theoretical basis document. Jet Propulsion Laboratory, California Institute of Technology, JPL Publication 12–17, August, 2012 (updated: March, 2014).

Hulley, G.C., Hughes, C.G., Hook, S.J., 2012b. Quantifying uncertainties in land surface temperature and emissivity retrievals from ASTER and MODIS thermal infrared data. J. Geophys. Res.-Atmos. 117 (n/a-n/a).

Hulley, G., Veraverbeke, S., Hook, S., 2014. Thermal-based techniques for land cover change detection using a new dynamic MODIS multispectral emissivity product (MOD21). Remote Sens. Environ. 140, 755–765.

Inoue, Y., Olioso, A., Choi, W., 2004. Dynamic change of CO_2 flux over bare soil field and its relationship with remotely sensed surface temperature. Int. J. Remote Sens. 25, 1881–1892.

Jacob, F., Weiss, M., 2014. Mapping biophysical variables from solar and thermal infrared remote sensing: focus on agricultural landscapes with spatial heterogeneity. IEEE Geosci. Remote Sens. Lett. 11, 1844–1848.

Jacob, F., Petitcolin, F.o., Schmugge, T., Vermote, É., French, A., Ogawa, K., 2004. Comparison of land surface emissivity and radiometric temperature derived from MODIS and ASTER sensors. Remote Sens. Environ. 90, 137–152.

Jacob, F., Schmugge, T., Olioso, A., French, A., Courault, D., Ogawa, K., Petitcolin, F., Chehbouni, G., Pinheiro, A., Privette, J., 2008. Modeling and inversion in thermal infrared remote sensing over vegetated land surfaces. Advances in Land Remote Sensing. Springer, pp. 245–291.

Jiménez-Muñoz, J.C., Sobrino, J.A., Gillespie, A., Sabol, D., Gustafson, W.T., 2006. Improved land surface emissivities over agricultural areas using ASTER NDVI. Remote Sens. Environ. 103, 474–487.

Jiménez-Muñoz, J.C., Sobrino, J.A., Skokovic, D., Mattar, C., Cristobal, J., 2014. Land surface temperature retrieval methods from Landsat-8 thermal infrared sensor data. IEEE Geosci. Remote Sens. Lett. 11, 1840–1843.

Jimenez-Munoz, J.C., Sobrino, J.A., Mattar, C., Hulley, G., Gottsche, F.M., 2014. Temperature and emissivity separation from MSG/SEVIRI data. IEEE Trans. Geosci. Remote Sens. 52, 5937–5951.

Justice, C.O., Vermote, E., Townshend, J.R.G., DeFries, R., Roy, D.P., Hall, D.K., Salomonson, V.V., Privette, J.L., Riggs, G., Strahler, A., Lucht, W., Myneni, R.B., Knyazikhin, Y., Running, S.W., Nemani, R.R., Zhengming, W., Huete, A.R., Van Leeuwen, W., Wolfe, R.E., Giglio, L., Muller, J.P., Lewis, P., Barnsley, M.J., 1998. The Moderate Resolution Imaging Spectroradiometer (MODIS): land remote sensing for global change research. IEEE Trans. Geosci. Remote Sens. 36, 1228–1249.

Kalma, J., McVicar, T., McCabe, M., 2008. Estimating land surface evaporation: a review of methods using remotely sensed surface temperature data. Surv. Geophys. 29, 421–469.

Labarre, L., Caillault, K., Fauqueux, S., Malherbe, C., Roblin, A., Rosier, B., Simoneau, P., 2010. An Overview of MATISSE-v2.0. In (pp. 782802-782802-782810).

Labarre, L., Caillault, K., Fauqueux, S., Malherbe, C., Roblin, A., Rosier, B., Simoneau, P., Schweitzer, C., Stein, K., Wendelstein, N., 2011. MATISSE-v2.0: New Functionalities and Comparison With MODIS Satellite Images. In (pp. 80140Z-80140Z-80113).

Labed, J., Stoll, M.P., 1991. Angular variation of land surface spectral emissivity in the thermal infrared: laboratory investigations on bare soils. Int. J. Remote Sens. 12, 2299–2310.

Lagouarde, J.-P., Bach, M., Sobrino, J.A., Boulet, G., Briottet, X., Cherchali, S., Coudert, B., Dadou, I., Dedieu, G., Gamet, P., Hagolle, O., Jacob, F., Nerry, F., Olioso, A., Ottlé, C., Roujean, J.-l., & Fargant, G., 2013. The MISTIGRI thermal infrared project: scientific objectives and mission specifications. Int. J. Remote Sens. 34, 3437–3466.

Lesaignoux, A., Fabre, S., Briottet, X., 2013. Influence of soil moisture content on spectral reflectance of bare soils in the 0.4–14 μm domain. Int. J. Remote Sens. 34, 2268–2285.

Li, Z.-L., Wu, H., Wang, N., Qiu, S., Sobrino, J.A., Wan, Z., Tang, B.-H., Yan, G., 2012. Land surface emissivity retrieval from satellite data. Int. J. Remote Sens. 34, 3084–3127.

Li, Z.-L., Tang, B.-H., Wu, H., Ren, H., Yan, G., Wan, Z., Trigo, I.F., Sobrino, J.A., 2013. Satellite-derived land surface temperature: current status and perspectives. Remote Sens. Environ. 131, 14–37.

Louchart, X., Voltz, M., 2007. Aging effects on the availability of herbicides to runoff transfer. Environ. Sci. Technol. 41, 1137–1144.

Malenovský, Z., Rott, H., Cihlar, J., Schaepman, M.E., García-Santos, G., Fernandes, R., Berger, M., 2012. Sentinels for science: potential of sentinel-1, −2, and −3 missions for scientific observations of ocean, cryosphere, and land. Remote Sens. Environ. 120, 91–101.

Merlin, O., Chehbouni, A., 2004. Different approaches in estimating heat flux using dual angle observations of radiative surface temperature. Int. J. Remote Sens. 25, 275–289.

Mira, M., Schmugge, T.J., Valor, E., Caselles, V., Coll, C., 2009. Comparison of thermal infrared emissivities retrieved with the two-lid box and the TES methods with laboratory spectra. IEEE Trans. Geosci. Remote Sens. 47, 1012–1021.

Mira, M., Schmugge, T.J., Valor, E., Caselles, V., Coll, C., 2011. Analysis of ASTER emissivity product over an arid area in Southern New Mexico, USA. IEEE Trans. Geosci. Remote Sens. 49, 1316–1324.

Murphy, R., 2006. The NPOESS preparatory project. In: Qu, J., Gao, W., Kafatos, M., Murphy, R., Salomonson, V. (Eds.), Earth Science Satellite Remote Sensing. Springer, Berlin Heidelberg, pp. 182–198.
Neinavaz, E., Darvishzadeh, R., Skidmore, A.K., Groen, T.A., 2016a. Measuring the response of canopy emissivity spectra to leaf area index variation using thermal hyperspectral data. Int. J. Appl. Earth Obs. Geoinf. 53, 40–47.
Neinavaz, E., Skidmore, A.K., Darvishzadeh, R., Groen, T.A., 2016b. Retrieval of leaf area index in different plant species using thermal hyperspectral data. ISPRS J. Photogramm. Remote Sens. 119, 390–401.
Nerry, F., Stoll, M.-P., Pion, J.C., 1996. Infrared spectro-radiometry. In: Kerr, Y.H., Mahkmara, H., Meunier, J.C., Valero, T. (Eds.), CD-ROM 3, HSIS LERTS/CNES/ORSTOM, MEDIAS-FRANCE, Toulouse, France.
Norman, J.M., Becker, F., 1995. Terminology in thermal infrared remote sensing of natural surfaces. Agric. For. Meteorol. 77, 153–166.
Ogawa, K., Schmugge, T., Jacob, F., French, A., 2003. Estimation of land surface window (8–12 μm) emissivity from multi-spectral thermal infrared remote sensing — a case study in a part of Sahara Desert. Geophys. Res. Lett. 30 (n/a-n/a).
Ogawa, K., Schmugge, T., Rokugawa, S., 2008. Estimating broadband emissivity of arid regions and its seasonal variations using thermal infrared remote sensing. IEEE Trans. Geosci. Remote Sens. 46, 334–343.
Olioso, A., 1992. Simulation deséchanges d'énergie et de masse d'un couvert végétal dans le but de relier la transpiration et la photosynthèse aux mesures de réflectance et de température de surface. In (p. 264): Montpellier II.
Olioso, A., 1995. Simulating the relationship between thermal emissivity and the normalized difference vegetation index. Int. J. Remote Sens. 16, 3211–3216.
Olioso, A., Taconet, O., Mehrez, M.B., 1996. Estimation of heat and mass fluxes from IR brightness temperature. IEEE Trans. Geosci. Remote Sens. 34, 1184–1190.
Olioso, A., Inoue, Y., Ortega-Farias, S., Demarty, J., Wigneron, J.P., Braud, I., Jacob, F., Lecharpentier, P., OttlÉ, C., Calvet, J.C., Brisson, N., 2005. Future directions for advanced evapotranspiration modeling: Assimilation of remote sensing data into crop simulation models and SVAT models. Irrig. Drain. Syst. 19, 377–412.
Olioso, A., Soria, G., Sobrino, J., Duchemin, B., 2007. Evidence of low land surface thermal infrared emissivity in the presence of dry vegetation. IEEE Geosci. Remote Sens. Lett. 4, 112–116.
Olioso, A., Jacob, F., Lesaignoux, A., 2014. SAIL-Thermique: a model for land surface spectral emissivity in the thermal infrared. Evaluation and reassessment of the temperature-emissivity separation (TES) algorithm in presence of vegetation canopies. AGU Fall Meeting Abstracts, p. 0461.
Pardo, N., Sánchez, M.L., Timmermans, J., Su, Z., Pérez, I.A., García, M.A., 2014. SEBS validation in a Spanish rotating crop. Agric. For. Meteorol. 195–196, 132–142.
Payan, V., Royer, A., 2004. Analysis of temperature emissivity separation (TES) algorithm applicability and sensitivity. Int. J. Remote Sens. 25, 15–37.
Petitcolin, F., Vermote, E., 2002. Land surface reflectance, emissivity and temperature from MODIS middle and thermal infrared data. Remote Sens. Environ. 83, 112–134.
R Development Core Team, 2011. R: A Language and Environment for Statistical Computing. the R Foundation for Statistical Computing, Vienna, Austria.
Ren, H., Liu, R., Yan, G., Li, Z.-L., Qin, Q., Liu, Q., Nerry, F., 2015. Performance evaluation of four directional emissivity analytical models with thermal SAIL model and airborne images. Opt. Express 23, A346–A360.
Rock, G., Gerhards, M., Schlerf, M., Hecker, C., Udelhoven, T., 2016. Plant species discrimination using emissive thermal infrared imaging spectroscopy. Int. J. Appl. Earth Obs. Geoinf. 53, 16–26.
Roy, D.P., Wulder, M.A., Loveland, T.R., W., C.E., Allen, R.G., Anderson, M.C., Helder, D., Irons, J.R., Johnson, D.M., Kennedy, R., Scambos, T.A., Schaaf, C.B., Schott, J.R., Sheng, Y., Vermote, E.F., Belward, A.S., Bindschadler, R., Cohen, W.B., Gao, F., Hipple, J.D., Hostert, P., Huntington, J., Justice, C.O., Kilic, A., Kovalskyy, V., Lee, Z.P., Lymburner, L., Masek, J.G., McCorkel, J., Shuai, Y., Trezza, R., Vogelmann, J., Wynne, R.H., Zhu, Z., 2014. Landsat-8: science and product vision for terrestrial global change research. Remote Sens. Environ. 145, 154–172.
Sabol, J.D.E., Gillespie, A.R., Abbott, E., Yamada, G., 2009. Field validation of the ASTER temperature–emissivity separation algorithm. Remote Sens. Environ. 113, 2328–2344.
Schmit, T.J., Gunshor, M.M., Menzel, W.P., Gurka, J.J., Li, J., Bachmeier, A.S., 2005. Introducing the next-generation advanced baseline imager on GOES-R. Bull. Am. Meteorol. Soc. 86, 1079–1096.
Schmugge, T., Hook, S.J., Coll, C., 1998. Recovering surface temperature and emissivity from thermal infrared multispectral data. Remote Sens. Environ. 65, 121–131.
Schmugge, T., French, A., Ritchie, J.C., Rango, A., Pelgrum, H., 2002. Temperature and emissivity separation from multispectral thermal infrared observations. Remote Sens. Environ. 79, 189–198.
Schröder, W., Schmidt, G., Hasenclever, J., 2006. Geostatistical analysis of data on AIR temperature and plant phenology from Baden-Württemberg (GERMANY) as a basis for regional scaled models of climate change. Environ. Monit. Assess. 120, 27–43.
Simoneau, P., Caillault, K., Fauqueux, S., Huet, T., Krapez, J.C., Labarre, L., Malherbe, C., Miesch, C., Roblin, A., Rosier, B., 2006. MATISSE: Version 1.4 and Future Developments. In (pp. 62390I-62390I-62397).
Sobrino, J.A., Jiménez-Muñoz, J.C., 2014. Minimum configuration of thermal infrared bands for land surface temperature and emissivity estimation in the context of potential future missions. Remote Sens. Environ. 148, 158–167.
Sobrino, J.A., Romaguera, M., 2004. Land surface temperature retrieval from MSG1-SEVIRI data. Remote Sens. Environ. 92, 247–254.
Sobrino, J.A., Jiménez-Muñoz, J.C., Balick, L., Gillespie, A.R., Sabol, D.A., Gustafson, W.T., 2007. Accuracy of ASTER level-2 thermal-infrared standard products of an agricultural area in Spain. Remote Sens. Environ. 106, 146–153.
Verhoef, W., 1984. Light scattering by leaf layers with application to canopy reflectance modeling: the SAIL model. Remote Sens. Environ. 16, 125–141.
Verhoef, W., 1985. Earth observation modeling based on layer scattering matrices. Remote Sens. Environ. 17, 165–178.
Verhoef, W., Jia, L., Qing, X., Su, Z., 2007. Unified optical-thermal four-stream radiative transfer theory for homogeneous vegetation canopies. IEEE Trans. Geosci. Remote Sens. 45, 1808–1822.
Vinukollu, R.K., Wood, E.F., Ferguson, C.R., Fisher, J.B., 2011. Global estimates of evapotranspiration for climate studies using multi-sensor remote sensing data: evaluation of three process-based approaches. Remote Sens. Environ. 115, 801–823.
Wan, Z., Li, Z.-L., 1997. A physics-based algorithm for retrieving land-surface emissivity and temperature from EOS/MODIS data. IEEE Trans. Geosci. Remote Sens. 35, 980–996.
Weiss, M., Baret, F., 1999. Evaluation of canopy biophysical variable retrieval performances from the accumulation of large swath satellite data. Remote Sens. Environ. 70, 293–306.
Weiss, M., Baret, F., Smith, G.J., Jonckheere, I., Coppin, P., 2004. Review of methods for in situ leaf area index (LAI) determination: part II. Estimation of LAI, errors and sampling. Agric. For. Meteorol. 121, 37–53.
Yamaguchi, Y., Kahle, A.B., Tsu, H., Kawakami, T., Pniel, M., 1998. Overview of Advanced Spaceborne Thermal Emission and Reflection Radiometer (ASTER). IEEE Trans. Geosci. Remote Sens. 36, 1062–1071.
Zhang, Y., Wan, Z., 1999. MODIS UCSB Emissivity Library. http://www.icess.ucsb.edu/modis/EMIS/html/em.html.